2D NUMERICAL FLOW MODELING IN A MACRO-ROUGH CHANNEL

Sébastien Erpicum
Research unit of Hydrology, Applied Hydrodynamics and Hydraulic Constructions (HACH),
ArGEnCo Department – MS²F – University of Liege (ULg)
Chemin des Chevreuils, 1 B52/3 B-4000 Liege, Belgium
e-mail: S.Erpicum@ulg.ac.be
tel: 00 32 4 366 95 96
fax : 00 32 4 366 95 58

Tobias Meile
Laboratory of Hydraulic Constructions (LCH),
Ecole Polytechnique Fédérale de Lausanne (EPFL)
Station 18, CH-1015 Lausanne, Switzerland

Benjamin Dewals
Belgian National Fund for Scientific Research FRS - FNRS
Research unit of Hydrology, Applied Hydrodynamics and Hydraulic Constructions (HACH),
ArGEnCo Department – MS²F – University of Liege (ULg)
Chemin des Chevreuils, 1 B52/3 B-4000 Liege, Belgium

Michel Pirotton
Research unit of Hydrology, Applied Hydrodynamics and Hydraulic Constructions (HACH),
ArGEnCo Department – MS²F – University of Liege (ULg)
Chemin des Chevreuils, 1 B52/3 B-4000 Liege, Belgium

Anton J. Schleiss
Laboratory of Hydraulic Constructions (LCH),
Ecole Polytechnique Fédérale de Lausanne (EPFL)
Station 18, CH-1015 Lausanne, Switzerland

1. Introduction

Most of the flows occurring in rivers and channels, even highly transient, can be reasonably seen as shallow, except in the vicinity of some singularities, as for example weirs. Indeed, vertical velocity components remain generally low compared to velocity components in the horizontal plane. Such flows may be considered as quasi two-dimensional. A depth integrated approach for flow modeling, taking into account a hydrostatic pressure distribution, is therefore suitable for many problems encountered in river, especially when modeling flows in channels with rather flat bottom.

It is generally assumed that turbulence effects might be neglected in many practical engineering applications, especially if external forces due to the solid boundary friction are predominant (steady flow) or if major advection effects are present (unsteady flow). However, the predominance of transport terms in the hydrodynamic equations can be less important, mainly in low velocity flows, close to hydraulic structures or for specific geometrical configurations [1, 2] which leads to an increasing effect of recirculation currents and velocity gradients.

Various approaches exist to handle turbulence in mathematical models, starting from direct numerical simulations (DNS) to large eddy simulations (LES) and mean flow variables simulations [3]. The modeling approach presented hereafter is based on a Reynolds averaging of the instantaneous flow variables. The new fluctuation terms in the resulting Reynolds averaged equations, called the Reynolds stresses, should be modeled by applying a proper turbulence model. For shallow water equations, several approaches are proposed in the literature, as rather simple algebraic expressions of turbulent viscosity [4 ,5] or more complex models with 1 or 2 additional equations [6, 7, 8].

In this paper, a new two-length-scale depth-integrated k-ε type model, involving two additional partial differential equations, is presented. This turbulence model integrated into shallow water equations [2] already proved to be relevant on test cases from the literature such as for a flow through a sudden enlargement [9] and in a channel with a groin [10]. In the present paper, this mathematical model is applied to another test case namely to backwater-curve computations in a laboratory channel with large scale cavity roughness at both channel banks [11, 12].

Such geometrical arrangements of river banks are used as a solution to mitigate the negative effects of hydro-peaking downstream of high head hydropower plants. They contribute to reduce peak discharge and water depth variations. The reliable numerical computation of steady states in such modified channels is a first step towards further analysis of transient flows and thus to systematic design of real arrangements.

The geometrical configurations of macro-roughness investigated with systematic hydraulic model tests produce recirculation zones, vertical mixing layers and wakes due to high velocity gradients in the main flow plane [11]. These flow characteristics are closely related to turbulence generation/dissipation and transport effects, particularly regarding head losses through turbulent friction in the shear layer and wake dissipation. They constitute thus a true challenge for numerical flow modeling.

2. Numerical model

2.1 Mathematical model

The flow model is based on the two-dimensional depth-averaged equations of volume and momentum conservation (Shallow Water Equations - SWE). In the “shallow-water” approach, it is assumed that velocities normal to a main flow plane are significantly smaller than those in the main flow direction. Consequently, the pressure field is almost hydrostatic everywhere.

A two-length-scale turbulence modeling approach is used, as described for example by Babarutsi and Chu [13]. It is well suited for applications where the water depth is small

compared to the horizontal dimensions of the flow and thus for SWE. The large-scale transverse-shear-generated turbulence, associated to the horizontal length-scale of the flow, and the small-scale bed-generated turbulence having a characteristic dimension in the order of magnitude of the water depth, are considered separately. This approach is based on the assumption that large scale velocity fluctuations are confined in the main flow plane, between the channel bottom and the free surface, while the small scale fluctuations are three-dimensional [13].

This assumption is consistent with the shallow water approach, where the depth-averaged velocity components in a main flow plane, i.e. the velocity components due to confined large-scale fluctuations, are computed explicitly.

The turbulence modeling is performed following a two-step Reynolds averaging procedure of the equations of motion, as suggested by Babarutsi and Chu [13]. The first stage filters out the bed-generated turbulence by treating the small scale fluctuations of the instantaneous three-dimensional velocity components with an algebraic model. The second stage considers the transverse-shear-generated turbulence by means of additional fluctuations of the mean velocity components in the main flow plane, modeled by two additional transport equations: one for the depth-averaged turbulent kinetic energy k', and one for the depth-averaged turbulence dissipation rate ε'.

Following analytical developments, the new final form of the depth-averaged equations of mass and momentum conservation together with the depth-averaged kinetic energy and dissipation rate transport equations can be written using vector notations as follows [2]:

$$\frac{\partial \mathbf{s}}{\partial t}+\frac{\partial \mathbf{f}}{\partial x}+\frac{\partial \mathbf{g}}{\partial y}+\frac{\partial \mathbf{f}_d}{\partial x}+\frac{\partial \mathbf{g}_d}{\partial y}=\mathbf{S} \tag{1}$$

where $\mathbf{s}=\begin{bmatrix} h & hu & hv & k' & \varepsilon' \end{bmatrix}^{\mathrm{T}}$ is the vector of the conservative unknowns. **f** and **g** represent the advective and pressure fluxes in directions *x* and *y*, while $\mathbf{f}_d$ and $\mathbf{g}_d$ are the diffusive fluxes and **S** is the vector of the source and non-conservative terms:

$$\mathbf{f}=\begin{pmatrix} hu \\ hu^2+\frac{1}{2}gh^2+k' \\ huv \\ uk' \\ u\varepsilon' \end{pmatrix},\ \mathbf{g}=\begin{pmatrix} hv \\ huv \\ hv^2+\frac{1}{2}gh^2+k' \\ vk' \\ v\varepsilon' \end{pmatrix} \tag{2}$$

$$\mathbf{f}_{\mathrm{d}}=-\begin{pmatrix} 0 \\ h\tau_{xx} \\ h\tau_{xy} \\ \frac{\nu^*}{h}\frac{\partial k'h}{\partial x}+\frac{\nu_{T,2D}}{\sigma_k}\frac{\partial k'}{\partial x} \\ \frac{\nu^*}{h}\frac{\partial \varepsilon'h}{\partial x}+\frac{\nu_{T,2D}}{\sigma_\varepsilon}\frac{\partial \varepsilon'}{\partial x} \end{pmatrix},\ \mathbf{g}_{\mathrm{d}}=-\begin{pmatrix} 0 \\ h\tau_{yx} \\ h\tau_{yy} \\ \frac{\nu^*}{h}\frac{\partial k'h}{\partial y}+\frac{\nu_{T,2D}}{\sigma_k}\frac{\partial k'}{\partial y} \\ \frac{\nu^*}{h}\frac{\partial \varepsilon'h}{\partial y}+\frac{\nu_{T,2D}}{\sigma_\varepsilon}\frac{\partial \varepsilon'}{\partial y} \end{pmatrix} \tag{3}$$

$$\mathbf{S}=\begin{pmatrix} 0 \\ -gh\dfrac{\partial z_b}{\partial x}+ghJ_x \\ -gh\dfrac{\partial z_b}{\partial y}+ghJ_y \\ -k'\dfrac{\partial u}{\partial x}-k'\dfrac{\partial v}{\partial y}+P'-F'-\dfrac{\varepsilon'}{h} \\ c_{1\varepsilon}\dfrac{\varepsilon'}{k'}\left[P'-\left(1-c_{3\varepsilon}\right)F'\right]-c_{2\varepsilon}\dfrac{\varepsilon'^2}{hk'} \end{pmatrix} \tag{4}$$

In equations (1) to (4), t represents the time, x and y the space coordinates, h the water depth, u and v the depth-averaged velocity components, z_b the bottom elevation, g the gravity acceleration, J_x and J_y the bottom slopes, τ_{xx} and τ_{yy} the viscous and turbulent normal stresses, τ_{xy} and τ_{yx} the viscous and turbulent shear stresses. $\nu^* = \nu + \nu_{T,3D}$ is the sum of the water viscosity ν and of the eddy viscosity $\nu_{T,3D}$ related to the bed-generated turbulence and $\nu_{T,2D}$ the eddy viscosity related to the large-scale transverse-shear-generated turbulence.

The bottom friction is conventionally modeled with an empirical law, such as the Manning formula. In addition, the friction along side walls is reproduced through a process-oriented formulation proposed by Dewals [1]. Finally friction terms become:

$$J_x = u\left[\sqrt{u^2+v^2}\,\frac{n_b^2}{h^{4/3}}+u\sum_{k_x=1}^{N_x}\frac{4}{3}\frac{n_w^2}{h^{1/3}\Delta y}\right] \tag{5}$$

and $$J_y = v\left[\sqrt{u^2+v^2}\,\frac{n_b^2}{h^{4/3}}+v\sum_{k_y=1}^{N_y}\frac{4}{3}\frac{n_w^{3/2}}{h^{1/3}\Delta x}\right] \tag{6}$$

where the Manning coefficients n_b and n_w characterize respectively the bottom and the side-walls roughness. These relations have been written for Cartesian grids used in the present study.

The production term of turbulence by the transverse shear and the term reflecting the effect of bottom friction forces on the turbulence motion are given by equations (7) and (8). The later has been derived as suggested by Babarutsi and Chu [13].

$$P' = \nu_{T,2D}\left[\left(\partial_x uh-\partial_y vh\right)\left(\partial_x u-\partial_y v\right)+\left(\partial_y uh+\partial_x vh\right)\left(\partial_y u+\partial_x v\right)\right] \tag{7}$$

$$F' = \frac{gn_b^2}{h^{4/3}}\left(3k'\sqrt{u^2+v^2}-\nu_{T,2D}\,\frac{\left(\partial_x uh-\partial_y vh\right)\left(u^2-v^2\right)+2\left(\partial_y uh+\partial_x vh\right)uv}{\sqrt{u^2+v^2}}\right) \tag{8}$$

The viscous and turbulent stresses τ_{ij} are the sum of three terms representing the viscous effects τ_{ij}^V, the bed-generated turbulence contribution $\tau_{ij}^{T,3D}$ and the large-scale transverse-shear-generated turbulence one $\tau_{ij}^{T,2D}$.

In the momentum equations, the viscous stresses are depth-averaged terms. In analogy with the general formulation for a Newtonian fluid, their gradients are modeled, for example along x-direction, as:

$$\partial_x h\tau_{xx}^V+\partial_y h\tau_{xy}^V = \nu\left(\partial_x^2 uh+\partial_y^2 uh\right) \tag{9}$$

The corresponding turbulent stresses gradients associated to bed-generated turbulence are modeled in the same manner, following an approach similar to the one of Chapmann and Kuo [14]:

$$\partial_x h\tau_{xx}^{T,3D} + \partial_y h\tau_{xy}^{T,3D} = \nu_{T,3D}\left(\partial_x^2 uh + \partial_y^2 uh\right) \tag{10}$$

The corresponding turbulent viscosity $\nu_{T,3D}$ is obtained based on a local equilibrium hypothesis [15], assuming equality between the production of turbulence by the bottom friction and its dissipation:

$$\nu_{T,3D} = c_\nu h U^* \tag{11}$$

where U^* is the bottom friction velocity and the value of the proportionality constant $c_\nu \simeq 0.08$ is recommended for non-stratified flows of uniform density over the depth [15].

In the same way, the turbulent stresses terms associated to large-scale transverse-shear-generated turbulence are modeled by a Boussinesq-type approximation. For example for *x*-momentum equation terms they write as:

$$h\tau_{xx}^{T,2D} = \nu_{T,2D}\left(\partial_x uh - \partial_y vh\right) - k' \tag{12}$$

$$h\tau_{xy}^{T,2D} = \nu_{T,2D}\left(\partial_y uh + \partial_x vh\right) \tag{13}$$

The associated turbulent viscosity $\nu_{T,2D}$ is evaluated according to Rodi [8] as a function of the turbulence variables k' and ε', transported by the main flow:

$$\nu_{T,2D} = c_\mu \frac{k'^2}{\varepsilon'} \tag{14}$$

The calculations are performed with a set of coefficients $\sigma_k = 1$, $\sigma_\varepsilon = 1.3$, $c_{1,\varepsilon} = 1.44$, $c_{2,\varepsilon} = 1.92$ and $c_\mu = 0.09$ assumed to be the same as for unconfined three-dimensional flow [15]. $c_{3,\varepsilon} = 0.8$ as proposed by Babarutsi and Chu [13] to model transverse mixing layer in shallow open-channel flows.

2.2 Grid and numerical scheme

The solver includes a mesh generator for a Cartesian grid. Compared to unstructured grids the main advantages of such structured grids are a lower computation time and a gain in accuracy. To overcome the main problem of Cartesian grids, i.e. the high number of cells needed for an enough fine discretization, multiblock features can increase the domain areas which can be discretized with a constant cells number and enable local mesh refinements near areas of interest [16].

The space of Eq. 1 is discretized with a finite volume scheme. This ensures a correct mass and momentum conservation, which is a must for handling properly discontinuous solutions such as moving hydraulic jumps. As a consequence, no assumption is required regarding the smoothness of the solution. Reconstruction at cell interfaces can be performed with a constant or linear approach. For the latter, together with slope limiting, a second-order spatial accuracy is obtained.

Appropriate flux computation has always been a challenging issue in computational fluid dynamics. The fluxes **f** and **g** are computed by a Flux Vector Splitting (FVS) method [2] where the upwinding direction of each term of the fluxes is simply dictated by the sign of the flow velocity reconstructed at the cells interfaces. It can be formally expressed as:

$$\mathbf{f}^{+}=\begin{pmatrix} hu \\ hu^2 \\ huv \\ uk' \\ u\varepsilon' \end{pmatrix} \quad ; \quad \mathbf{f}^{-}=\begin{pmatrix} 0 \\ gh^2/2+k' \\ 0 \\ 0 \\ 0 \end{pmatrix} \tag{15}$$

$$\mathbf{g}^{+}=\begin{pmatrix} hv \\ huv \\ hv^2 \\ vk' \\ v\varepsilon' \end{pmatrix} \quad ; \quad \mathbf{g}^{-}=\begin{pmatrix} 0 \\ 0 \\ gh^2/2+k' \\ 0 \\ 0 \end{pmatrix} \tag{16}$$

where the exponents + and - refer to, respectively, an upstream and a downstream evaluation of the corresponding terms. A stability analysis has shown that this FVS ensures a stable spatial discretization of the terms $\partial\mathbf{f}/\partial x$ and $\partial\mathbf{g}/\partial y$ in Eq. 1 [2]. Due to their diffusive character, the fluxes $\mathbf{f}_d$ and $\mathbf{g}_d$ can be determined by means of a centred scheme. The non-conservative terms are obtained in upstream direction by analogy with the corresponding advective terms.

Besides low computation costs, this FVS has the advantages of being completely Froude independent. Furthermore the adequacy of discretization of the bottom slope term is facilited [1, 2, 16, 17, 18].

2.3 Time discretization and boundary conditions

Since the model is applied to compute steady-state solutions, the time integration is performed by means of a 3-step first order accurate Runge-Kutta algorithm, providing adequate dissipation in time. For stability reasons, the time step is constrained by the Courant-Friedrichs-Levy condition based on gravity waves. The bottom friction term is treated semi-implicitly, without increasing computational time [1].

For each application, the value of the specific discharge can be fixed as an inflow boundary condition. The transverse specific discharge is usually set to zero at the inflow even if a different value can be used if necessary. In case of supercritical flow, a water surface elevation can be provided as additional inflow boundary condition.

The outflow boundary condition may be a water surface elevation, a Froude number or no specific condition if the outflow is supercritical. At solid walls, the component of the specific discharge normal to the wall is set to zero.

Regarding turbulence variables, the shear velocity on solid walls is computed according the law of the wall. The corresponding depth-averaged kinetic energy and dissipation rates are calculated, in analogy with Rodi [8] and Younus and Chaudhry [19], as respectively

$$k' = \frac{h\left(U^{\tau}\right)^2}{\sqrt{c_{\mu}}} \tag{17}$$

$$\varepsilon' = \frac{h^2\left(U^{\tau}\right)^3}{\kappa d} \tag{18}$$

where U^{τ} is the shear velocity assuming a logarithmic velocity profile near the wall, κ the von Karman constant and d the distance to the wall. Furthermore, this approach assumes that the laminar boundary layer is within the mesh next to the wall. At inlets, values of $k'_0 = 10^{-4}\, q_0^2/h$ and $\varepsilon'_0 = 10\, k_0'^{3/2}/\sqrt{h}$ are used [20] to link the turbulence variables intensity to the discharge boundary condition q_0.

3. Physical experiments and selected test cases

Hydraulic model tests of macro-rough channel configurations have been performed in a flume with a useful length of 38.33 m and a mean bed slope of 1.14 ‰ (Fig. 1). The channel is divided from upstream to downstream into an inlet reach (length 7.41 m), a reach with large scale cavity roughness at the banks (26.92 m) and an outlet reach (4.0 m). The channel bottom is made of painted steel. The sidewalls of the inlet reach are constructed by wooden boards. The sidewalls of the reach including the large scale depressions, namely rectangular cavities, and the outlet reach are formed by smooth limestone bricks. The channel bed is fixed and no sediment transport is taken into account.

The channel base width is $B = 0.485 \pm 0.002$ m and remained constant during all the tests. Three geometrical parameters namely the length of the cavity L_b, the distance between two cavities L_c and the depth of the cavities ΔB, have been systematically varied (Fig. 1). Table 1 summarizes the range of the investigated geometrical parameters L_b, L_c and ΔB as well as derived ratios such as the aspect and expansion ratios of the cavity defined as $AR = \Delta B / L_b$ and $ER = (B + 2\Delta B) / B$ respectively. The combination of three different values for L_b and L_c and four different values of ΔB results in 36 different, axi-symmetric geometrical configurations covering 8 aspect and 4 expansion ratios. Additionally, a prismatic and a randomly generated configuration have been analyzed [11].

Four out of the 36 different geometrical configurations (Fig. 2) have been selected to be investigated with the numerical model for various discharges (Table 2). Furthermore, the prismatic channel served as reference for the calibration for the bottom and wall surface roughness.

The choice of the test cases is motivated by the different cavity flow types identified in the experimental study [11] namely the square grooved flow type (conf. 124), the reattachment flow type (conf. 221) and the normal recirculating flow type (conf. 121 and 224).

The discharge during the tests was controlled by an electromagnetic flow meter. The water levels have been recorded with ultrasonic elevation probes located along the channel axis. The accuracy of the measurements is at least ± 0.002 m. The ultrasonic elevation probes have been placed in the small channel sections or at the beginning, in the middle and at the end of the widened channel reaches (Fig. 2). Thus, variations of the flow depth at specific locations can be evaluated.

The discharge is introduced at the upstream border of the channel through a horizontal opening of the inlet basin. At the downstream border of the channel, the flow depth is controlled by a particularly shaped cross section. It corresponds almost to the normal flow depth of the prismatic channel without macro-roughness.

Characteristic values of Froude $Fr = U \cdot (g \cdot h)^{-1}$ and Reynolds $Re = U \cdot R_h \cdot \nu^{-1}$ numbers relative to the base width B ranged between $0.37 < Fr < 0.64$ and $6'800 < Re < 110'000$ for typical flow depths between $0.03\ \text{m} < h < 0.34\ \text{m}$ and mean flow velocities between $0.24\ \text{ms}^{-1} < U < 0.80\ \text{ms}^{-1}$. U is the mean flow velocity in the cross-section and R_h is the hydraulic radius, both calculated relative to the small channel section at base width B.

4. Results

4.1 Prismatic channel

First the prismatic channel has been modeled both experimentally and numerically for discharges of *0.278 m^2/s* and *0.0133 m^2/s* in order to fit the Manning's roughness coefficients n_b and n_w value in the numerical model. Regarding the surface materials of the flume, i.e. painted steel and limestone bricks, the values of n_b and n_w have been considered constant along the channel bottom and the side walls respectively.

A mesh size of *0.02 m* has been used to model a length of *34.22 m* of the channel of constant width (*0.48 m*). The values of the free water surface elevation measured at a downstream probe in the experimental facility have been used as the downstream boundary conditions.

The constant specific discharges injected in the channel constitute the upstream ones. The measurements realized on nine ultrasonic elevation probes, regularly spaced along the channel (Fig. 2), have been used for the comparison to the numerical results.
The best balance between bottom and sidewall friction has been found to be $n_b=0.0087\ s/m^{1/3}$ and $n_w=0.0105\ s/m^{1/3}$. The sidewalls are rougher than the bottom, in agreement with the experimental facility materials surface patterns. These values have been definitively validated by the comparison of the numerical results with the experimental measurements for seven additional discharges between $0.219\ m^2/s$ and $0.0275\ m^2/s$ (Fig. 3, Table 3 and Table 4).

4.2 Macro-rough channels

In a second stage, four configurations with large scale depression roughness at the side walls (Fig. 2 and Table 2) have been modeled. The same mesh size of *0.02 m* has been used to model a length of *36.32 m* of the channel. The width varies along the channel, depending on the geometrical configurations. The only numerical model parameters are the roughness coefficients previously found from the calibration tests in the prismatic channel ($n_b=0.0087\ s/m^{1/3}$ and $n_w=0.0105\ s/m^{1/3}$).
The free surface elevations measured at the downstream probe have again been used as the downstream boundary conditions. Constant specific discharges injected in the channel constitute the upstream ones. The free surface elevation measured with 25 ultrasonic elevation probes located at the channel axis along the experimental flume have been used for the assessment of the accuracy of the numerical results (Fig. 2).
The backwater curves of the configuration with reattachment of the flow to the side walls are very well reproduced. The difference between the measured and computed water depths is in the order of magnitude of the probes accuracy and less than 2% for the higher discharges (Fig. 4, Table 3 and Table 4). The configurations with normal recirculating flow type are also satisfactory reproduced for the aspect ratio $\Delta B/L_b$ equal to 0.2 and a little less for $\Delta B/L_b$ equal to 0.4. The configuration governed by a square grooved flow type shows a difference between measured and computed flow depths reading 15% for the higher discharges. Furthermore the computed flow depths are underestimated by 0.025 m in maximum.
Additional simulations of the first two axi-symmetric cavities have been carried out in each configuration with a mesh size of *0.01 m* in order to get a finer modeling of the flow pattern inside the cavities. The boundary conditions have been taken from the simulations along the whole channel.

5. Discussion

5.1 Importance of turbulence modeling

In 2D flow solvers, the turbulence terms in the momentum equations play an important role on external friction modeling, especially when the friction along the side walls can not be neglected. Without using any turbulence model, the velocity distribution over the channel width is rather uniform with a sudden local decrease along rough side walls (Fig. 5), and the velocity gradient is counterbalanced only by pressure gradients. Considering the turbulence terms in the momentum equations, this high velocity gradient along the side walls is in addition also counterbalanced by transverse shear stresses. Thus, the velocity distribution is more gradual (Fig. 5).
The velocity distribution directly influences the roughness terms and thus the head losses. Without using a turbulence model and when considering a high roughness of the side walls compared to the bottom roughness, the velocity remains small in the meshes close to the side walls. Thus, the influence of side walls on the head losses is small even if they are very rough. Therefore it was not possible to fit the roughness coefficients in the prismatic channel using the 2D flow model without any turbulence terms, despite a good representation of the side walls friction effect. A first set of friction coefficients ($n_b = 0.01\ s/m^{1/3} – n_w = 0.0125\ s/m^{1/3}$)

has been used to compute the backwater curves for the discharges q_1 and q_9 without using turbulence terms. The obtained backwater curves in Fig. 6 reveal that the bottom roughness should slightly be decreased and the side wall roughness strongly increased in order to fit the measured water depths along the channel. For the second set of friction coefficients (n_b = $0.0087\ s/m^{1/3}$ – $n_w = 0.02\ s/m^{1/3}$), despite a strong increase of the side wall roughness, the head loss along the channel generally decreases (Fig. 6) as the flow velocity along the side wall decreases. The local increase of the head loss at the upstream end of the channel is due to the discharge boundary condition assuming uniform velocity distribution over the channel width.
It may be concluded that without using turbulence terms in a 2D modeling approach, no set of roughness coefficients can be found to fit the water depth measurements for various discharges. This problem does not exist in 1D models where all friction terms in a cross section are computed from the mean flow velocity [11].

5.2 Flow patterns

In Figure 7, the experimental and numerical time averaged flow patterns are compared. Flow patterns have been qualitatively visualized during the experiments by the help of dye injection. A good agreement between numerical and physical results can be observed especially in the case of the reattachment flow type ($\Delta B/L_b \leq 0.1$), for which an elongated, triangular recirculation gyre develops next to the cavity leading edge. Good agreement of the flow patterns is also found for the square grooved flow type ($\Delta B/L_b \cong 0.8$) which is characterized by a single and almost circular gyre. For the normal recirculating flow type, the experiments indicate a recirculation of the flow with a primary and secondary gyre inside of the cavity as well as a slight expansion of the main flow streamlines into the cavity. The size of the secondary gyre might vary and it can become very small. Furthermore, in all cases, the secondary gyre is rotating with a much smaller velocity than the primary gyre [11]. In the numerical simulations the size of this secondary gyre is underestimated.
Transversal flow oscillations have been observed during the experiments for the test cases 124 and 224 in the widened channel reaches. For both configurations, the semi-confined water bodies are seiching with a frequency that can be predicted with the theory of sloshing in a rectangular basin [21]. Oscillations transverse to the main flow direction, coupled with alternating vortex shedding at the cavity leading edge, also occurred for the geometrical configurations 124 and 224 in the numerical simulations. However, the frequency is much lower in the numerical simulations.
The occurrence of these oscillations in the numerical model should be explained by an analysis of the computation process. Indeed, having a symmetrical geometry along the channel and uniform boundary conditions, non symmetric behavior can not be initiated by the numerical scheme. Despite a dissipative time integration scheme, the oscillations are amplified and reach a periodic behavior in configurations 124 and 224. On the other hand they are not amplified in any steady solution for configurations 121 and 221. This is in agreement with the experimental observations for which stable flow patterns have been observed in configurations 121 and 221.

5.3 Turbulent viscosity components

Figure 8 illustrates the evolution along the channel length of both the width-integrated bed generated (3D) and width-integrated transverse shear generated (2D) turbulent viscosity components. The 3D component, computed assuming equilibrium between production and dissipation, is rather constant along the channel axis. It is concentrated in the main channel (Fig 9), where the depth integrated velocities are maximum. Furthermore, the 3D turbulent viscosity components are very small in the cavities due to the small flow velocities. Finally, whatever the channel geometry, the amplitude of the width-integrated 3D turbulent viscosity component is rather constant for a certain discharge (Fig. 8).

The 2D turbulent viscosity is computed on the basis of two variables obtained from additional transport equations. From the 2D turbulent viscosity distribution (Fig. 10) two effects can be seen. First, in cavities with a low aspect ratio $\Delta B/L_b$, the 2D turbulent viscosity increases in the direction of the flow. In the cavities with high aspect ratios, it is distributed homogeneously. Secondly, the 2D turbulence increases due to transport in the main channel from upstream to downstream. The width integrated 2D turbulent viscosity increases along the macro-rough configuration and reaches an equilibrium level after a few widenings (Fig. 8). In cavities with a low aspect ratio $\Delta B/L_b$, the width integrated 2D turbulent viscosity increases linearly with the flow expansion up to a maximum which is reached at the sudden contraction, where the flow velocity gradients are maximum. In cavities with higher aspect ratio, the turbulent viscosity is more constant along the cavity since the velocity gradients are high in the vicinity of the recirculating gyre. Furthermore, in configuration 124, a local increase of the width-integrated 2D turbulent viscosity is observed due to the stagnation point.

5.4 Research perspectives

A way to further improve the numerical results is to change the value of the coefficients of the turbulence model. Tests have been carried out to assess the effect of bottom friction in the depth averaged dissipation equation by changing the $c_{3,\varepsilon}$ parameter value to 1 as suggested by Babarutsi [13]. At this stage, no significant change is seen on the numerical results. The influence of the parameter c_ν in eq. 11 should be analysed in a further step as it directly regulates the bed-generated turbulence intensity. There is less reason to modify the other parameters of turbulence equations as they are generally assumed as universal constants in the three-dimensional k-ε model. Nevertheless, their validity for the depth integrated approach described in this paper should be analysed properly.

Furthermore, to improve the flow patterns in the corners of the cavities, the boundary condition on the depth averaged kinetic energy and dissipation rate along side walls might be modified considering developments of Nassiri [22] for example. Finally, in the case of this specific application with quite low flow velocities in the cavities, other boundary friction laws than Manning could by applied.

6. Conclusions

A numerical flow model has been applied to flows in a macro-rough channel. The model solves the shallow water equations with a new two-length-scale depth integrated k-ε type turbulence modeling approach. Data for the comparison were obtained from experiments performed with different non prismatic channel configurations, namely large scale cavities at the side walls, and various discharges. Two dimensional flow features such as vertical mixing layers, wake zones and flow recirculation in cavities could be observed.

With 2D numerical model features, and especially considering turbulence modeling, a single set of bottom and side wall roughness for a large range of discharges investigated in a prismatic channel can be found. It is shown that this is not possible without turbulence terms in the momentum equations.

By the separation of 2D and 3D turbulence effects in the model, an excellent agreement between experimental and numerical results could be obtained regarding backwater curves and flow patterns in the macro-rough configurations with low aspect ratios. For configurations with high aspect ratios of the side wall cavities, the head losses generated by the important recirculation gyres are slightly underestimated.

Furthermore, the analysis of the turbulent viscosity in geometrical configurations with macro-roughness at side walls clearly shows the important part of the total turbulent viscosity related to 2D transverse shear effects compared to bed-generated 3D turbulence. Thus, in 2D flow numerical modeling, the amplitude of 3D, bed-generated turbulence, and 2D, transverse-shear-generated turbulence, can be very different. As a consequence, the separation of the

turbulence effects in the mathematical model makes it suitable to reproduce accurately most flow features depending on internal friction effects.

Acknowledgements
The experiments are part of a PhD thesis carried out within the Rhone-Thur national research project “Sustainable use of rivers” granted by the Swiss Federal Office for the Environment (FOEN). The velocity measurement equipment was supported by Met-Flow SA, Lausanne, Switzerland.

Notations

$AR = \Delta B / L_b$	aspect ratio of a cavity	[-]
B	channel base width	[L]
$c_\nu, c_\mu, c_{1,\varepsilon}, c_{2,\varepsilon}, c_{3,\varepsilon}$	constants of the turbulence model	[-]
d	distance to the wall	[L]
$ER = (B + 2\Delta B) / B$	expansion ratios of a cavity	[-]
$\mathbf{f}$	advective and pressure fluxes in direction x	
$\mathbf{f}_d$	diffusive fluxes in direction x	
F'	effect of bed-friction on turbulence motion	$[L^3T^{-2}]$
Fr	Froude number	[-]
g	gravity acceleration	$[LT^{-2}]$
$\mathbf{g}$	advective and pressure fluxes in direction y	
$\mathbf{g}_d$	diffusive fluxes in direction y	
h	water depth	[L]
J_x	bottom slope component along x-axis	[-]
J_y	bottom slope component along y-axis	[-]
k	turbulent kinetic energy	$[L^2T^{-2}]$
k'	depth-averaged turbulent kinetic energy	$[L^3T^{-2}]$
L_b	length of a cavity	[L]
L_c	distance between two cavities	[L]
n_b	Manning coefficient for bottom roughness	$[TL^{-1/3}]$
n_w	Manning coefficients for side-walls roughness	$[TL^{-1/3}]$
P'	production term of turbulence by the transverse shear	$[L^3T^{-2}]$
Re	Reynold number	[-]
R_h	hydraulic radius	[L]
$\mathbf{s}$	vector of the conservative unknowns	
$\mathbf{S}$	vector of the sink and non-conservative terms	
t	time	[T]
u	depth-averaged velocity component along x-axis	$[LT^{-1}]$
U	mean flow velocity in the cross-section	$[LT^{-1}]$
U^*	bottom friction velocity	$[LT^{-1}]$
U^τ	shear velocity	$[LT^{-1}]$
v	depth-averaged velocity component along y-axis	$[LT^{-1}]$
x	space coordinate	[L]
y	space coordinate	[L]
z_b	bottom elevation	[L]
ΔB	depth of the cavities	[L]
Δx	space discretization step along x-axis	[L]
Δy	space discretization step along y-axis	[L]

ε	turbulence dissipation rate	$[L^2T^{-3}]$
ε'	depth-averaged turbulence dissipation rate	$[L^4T^{-3}]$
κ	von Karman constant	[-]
ν^*	sum of the water viscosity ν and of the eddy viscosity $\nu_{T,3D}$	$[L^2T^{-1}]$
ν	water viscosity	$[L^2T^{-1}]$
$\nu_{T,3D}$	eddy viscosity related to the small scale bed-generated turbulence	$[L^2T^{-1}]$
$\nu_{T,2D}$	eddy viscosity related to the large-scale transverse-shear-generated turbulence	$[L^2T^{-1}]$
$\sigma_k, \sigma_\varepsilon$	constants of the turbulence model	[-]
τ_{xx} and τ_{yy}	viscous and turbulent normal stresses	$[L^2/T^{-2}]$
τ_{xy} and τ_{yx}	viscous and turbulent shear stresses	$[L^2/T^{-2}]$
τ_{ij}^V	components of τ_{ij} related to viscous effects	$[L^2/T^{-2}]$
$\tau_{ij}^{T,3D}$	components of τ_{ij} related to the bed-generated turbulence	$[L^2/T^{-2}]$
$\tau_{ij}^{T,2D}$	components of τ_{ij} related to the large-scale transverse-shear-generated turbulence	$[L^2/T^{-2}]$

References

1 Dewals BJ. *Une approche unifiée pour la modélisation d'écoulements à surface libre, de leur effet érosif sur une structure et de leur interaction avec divers constituants*. PhD Thesis, Unité d'Hydrodynamique Appliquée et des Constructions Hydrauliques, Université de Liège : Liège, 2006; 636 p.

2 Erpicum S. *Optimisation objective de paramètres en écoulements turbulents à surface libre sur maillage multibloc*. PhD Thesis, Unité d'Hydrodynamique Appliquée et des Constructions Hydrauliques, Université de Liège : Liège, 2006; 356 p.

3 Chassaing P. *Turbulence en mécanique des fluides – Analyse du phénomène en vue de sa modélisation par l'ingénieur*, Cépaduès :Toulouse, 2000; 625 p.

4 Fischer H, List E, Koh R, Imberger J, Brooks N. *Mixing in inland and coastal waters*. Academic Press: New York, 1979; 483 p.

5 Hervouet, J-M. *Hydrodynamique des écoulements à surface libre - Modélisation numérique avec la méthode des éléments finis*. Presses de l'Ecole Nationale des Ponts et Chaussées : Paris, 2003; 311 p.

6 Tennekes H, Lumley J. *A first course in turbulence*. MIT Press: Cambridge, 1972; 320 p.

7 Rastogi A, Rodi W. Predictions of heat and mass transfer in open channels. *Journal of the Hydraulics Division, ASCE* 1978; **104**(HY3): 397-420.

8 Rodi W. *Turbulence models and their application in hydraulics - A state-of-the-art (second revised edition)*. Balkema: Leiden, 1984; 104 p.

9 Babarutsi S, Ganoullis J, Chu VH. Experimental investigation of shallow recirculating flows. *Journal of Hydraulic Engineering* 1989; **115**(7): 906-924.

10 Rajaratnam N, Nwachukwu B. Flow near groin-like structures. *Journal of Hydraulic Engineering* 1983; **109**(3): 463-480.

11 Meile T. *Influence of macro-roughness of walls on steady and unsteady flow in a channel*. PhD thesis No 3952 of Ecole Polytechnique Fédérale de Lausanne and Communication No 36 of the Laboratory of Hydraulic Constructions (LCH-EPFL): Lausanne, 2007; 414 p. ISSN 1661-1179

12 Morris H, Wiggert J. *Applied hydraulics in engineering*, The Ronald Press Company: New York, 1972; 640 p.
13 Babarutsi S, Chu VH. Modeling transverse mixing layer in shallow open-channel flows. *Journal of Hydraulic Engineering* 1998; **124**(7): 718-727.
14 Chapman R, Kuo C. Application of the two-equation k-ε turbulence model to a two-dimensional, steady, free surface flow problem with separation. *International Journal for Numerical Methods in Fluids* 1985; **5**: 257-268.
15 Babarutsi S. *Modelling quasi-two-dimensionnal turbulent shear flow*. PhD Thesis, Civil Engineering and Applied Mechanics, Mc Gill University: Montreal, 1991; 140 p.
16 Erpicum S, Dewals BJ, Archambeau P, Detrembleur S, Pirotton M. Detailed 2D numerical modeling for flood extension forecasting. *Proc. of Riverflow 2008 Conference*: Izmir, Turkey, 2008; 2159-2168.
17 Dewals BJ, Erpicum S, Archambeau P, Detrembleur S, Pirotton M. Depth-integrated flow modelling taking into account bottom curvature. *Journal of Hydraulic Research* 2006; **44**(6): 787-795.
18 Dewals BJ, Kantoush S, Erpicum S, Pirotton M, Schleiss A. Experimental and numerical analysis of flow instabilities in rectangular shallow basins, *Environmental Fluid Mechanics* 2008; **8**: 31-54.
19 Younus M, Chaudhry M. A depth-averaged k-ε turbulence model for the computation of free-surface flow. *Journal of Hydraulic Research* 1994; **32**(3): 415-439.
20 Choi S-U, Garcia M. k-ε turbulence modelling of density currents developing two dimensionally on a slope. *Journal of Hydraulic Engineering* 2002; **128**(1): 55-63.
21 Meile T, Boillat J-L, Schleiss A. Water surface oscillations in a channel with axi-symmetric embayments. Submitted to *Experiments in Fluids*.
22 Nassiri M, Babarutsi S, Chu VH. Wall boundary conditions on recirculating flows dominated by bottom friction, *Proc. of XXVIII IAHR Congress*: Graz, Austria, 1999.

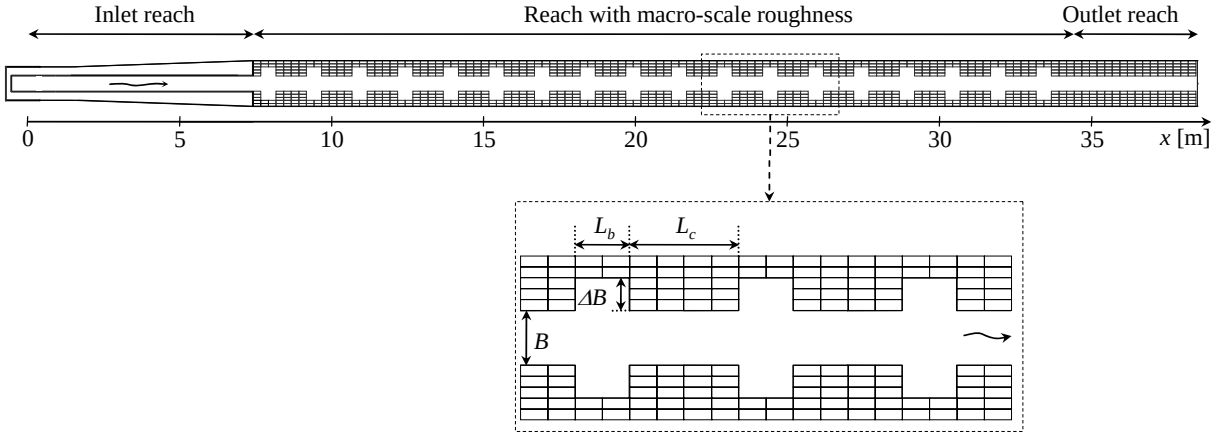

Figure 1: Plane view of the test flume (above) and definition of the parameters of the macro-rough geometrical configurations (below).

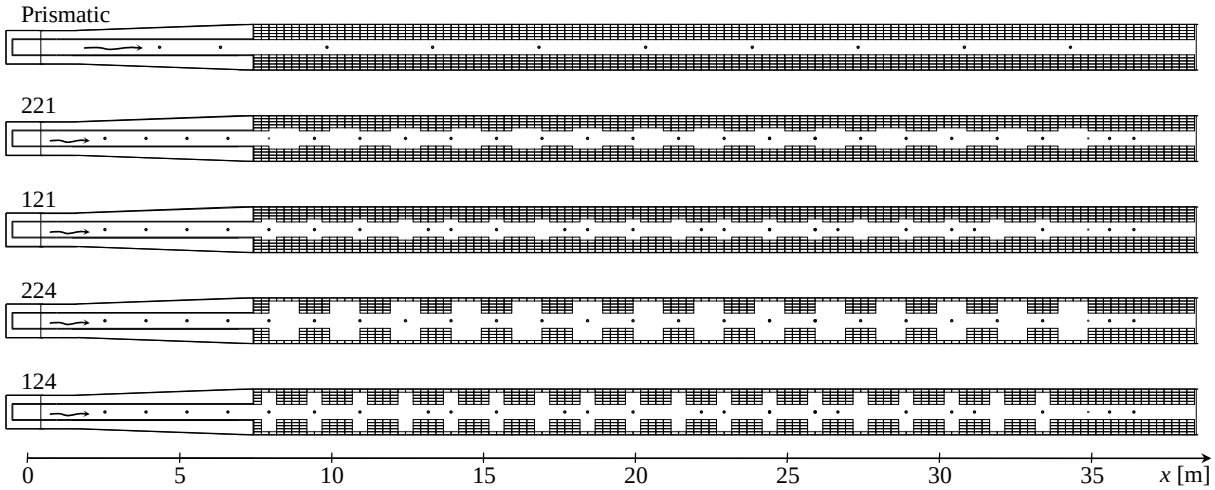

Figure 2: Prismatic and macro-rough test cases. The positions of the ultrasonic elevation probes along the channel axis are indicated with ●.

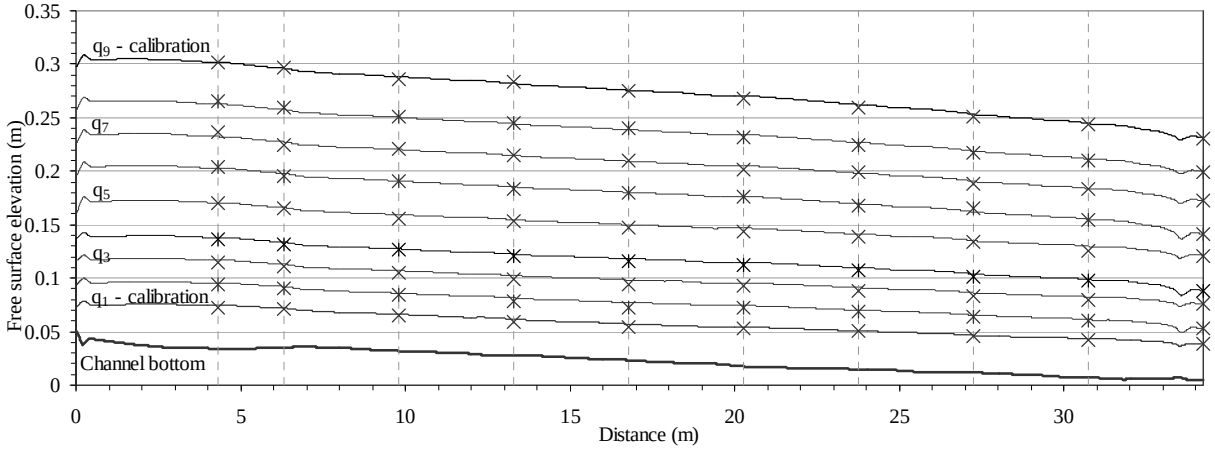

Figure 3: Comparison of experimental and simulated backwater curves in the prismatic reference configuration for nine different specific discharges q in the channel.

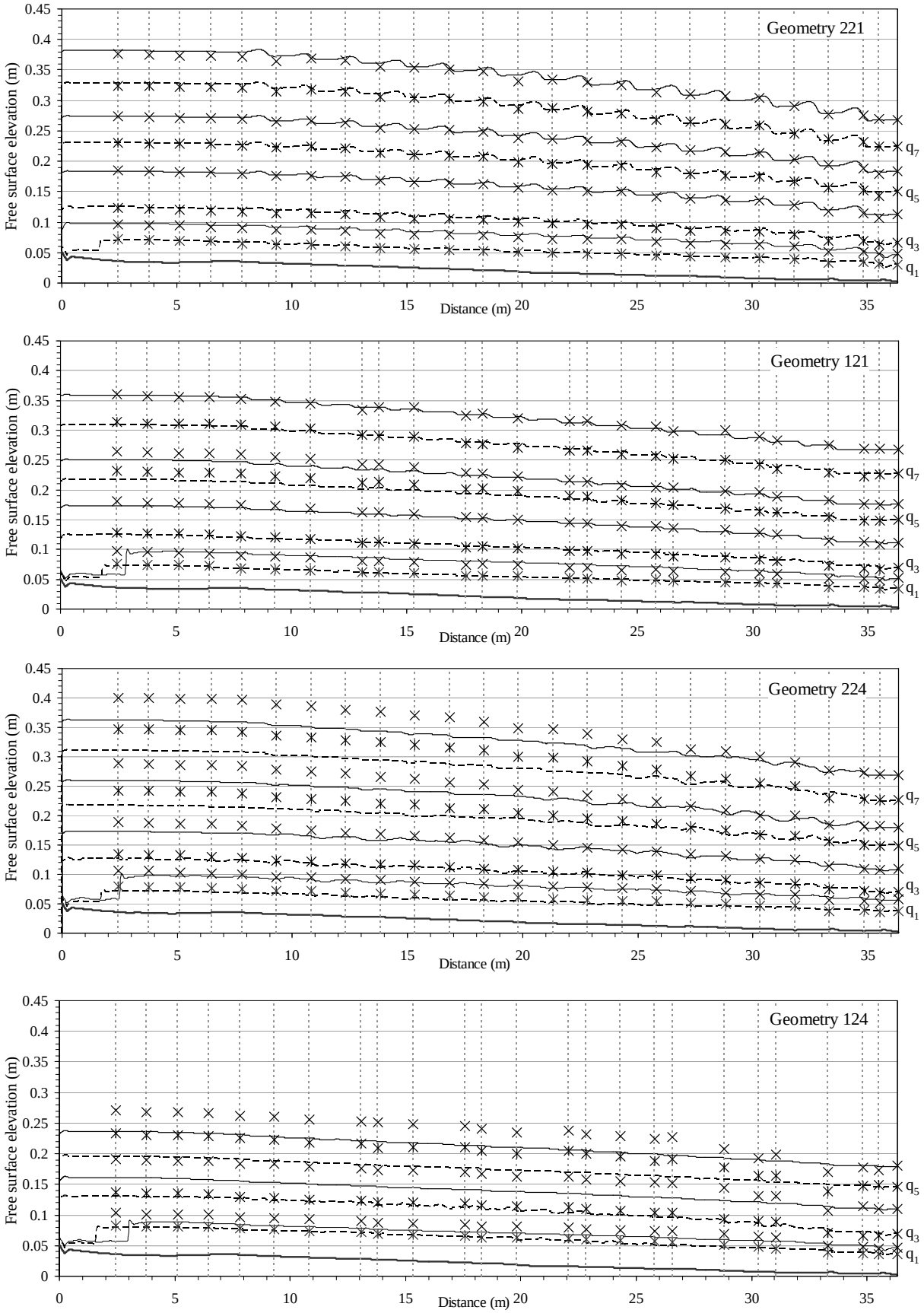

Figure 4: Comparison of experimental and simulated backwater curves for different specific discharges q in the channel for the configurations with large scale depression roughness at the side walls.

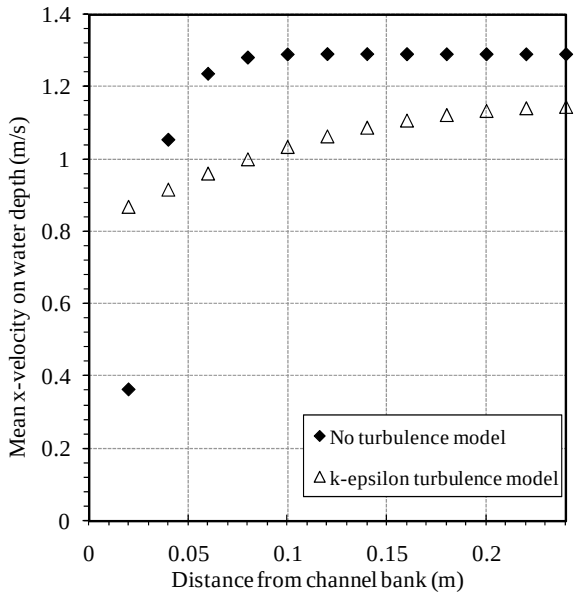

Figure 5: Streamwise velocity components with and without turbulence model.

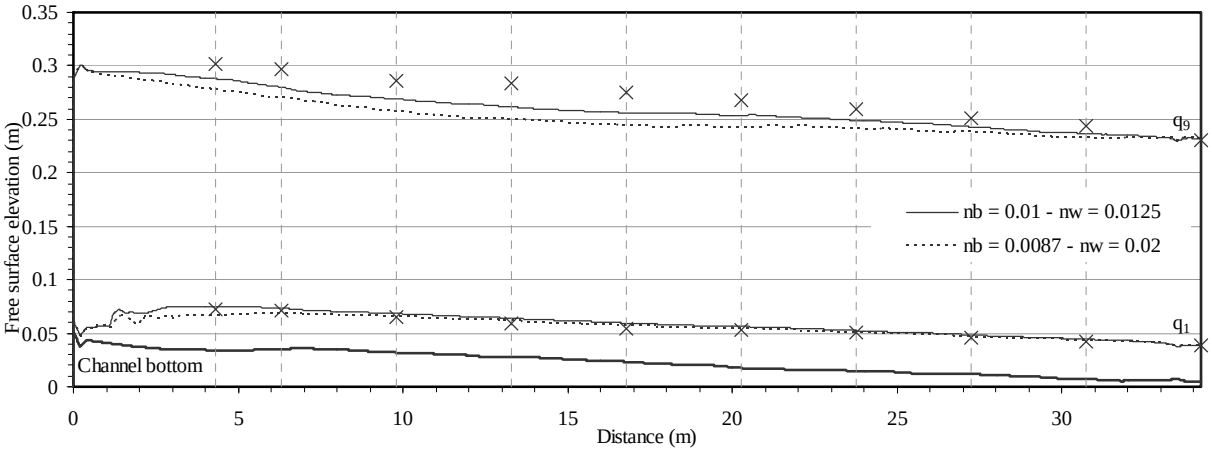

Figure 6: Backwater curve computations in the prismatic channel without turbulence model. q is the specific discharge in the channel, nb *is the bottom roughness coefficient and* nw *is the side walls roughness coefficient*

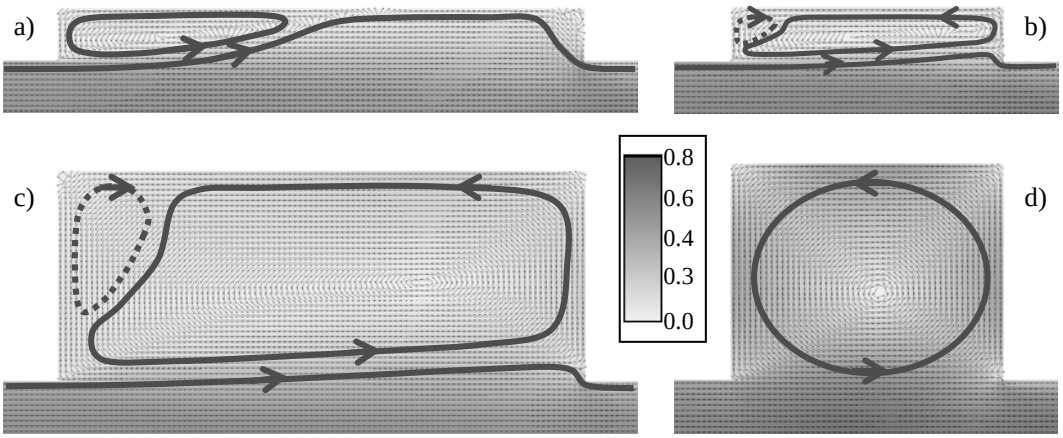

Figure 7: Cavity flow patterns for the configurations with large scale roughness (Flow velocity in m/s). Discharge is q_4 according to table 2. (a) 221, flow reattachment. (b) 121, normal recirculating flow type. (c) 224, normal recirculating flow type. (d) 124, square grooved flow type.

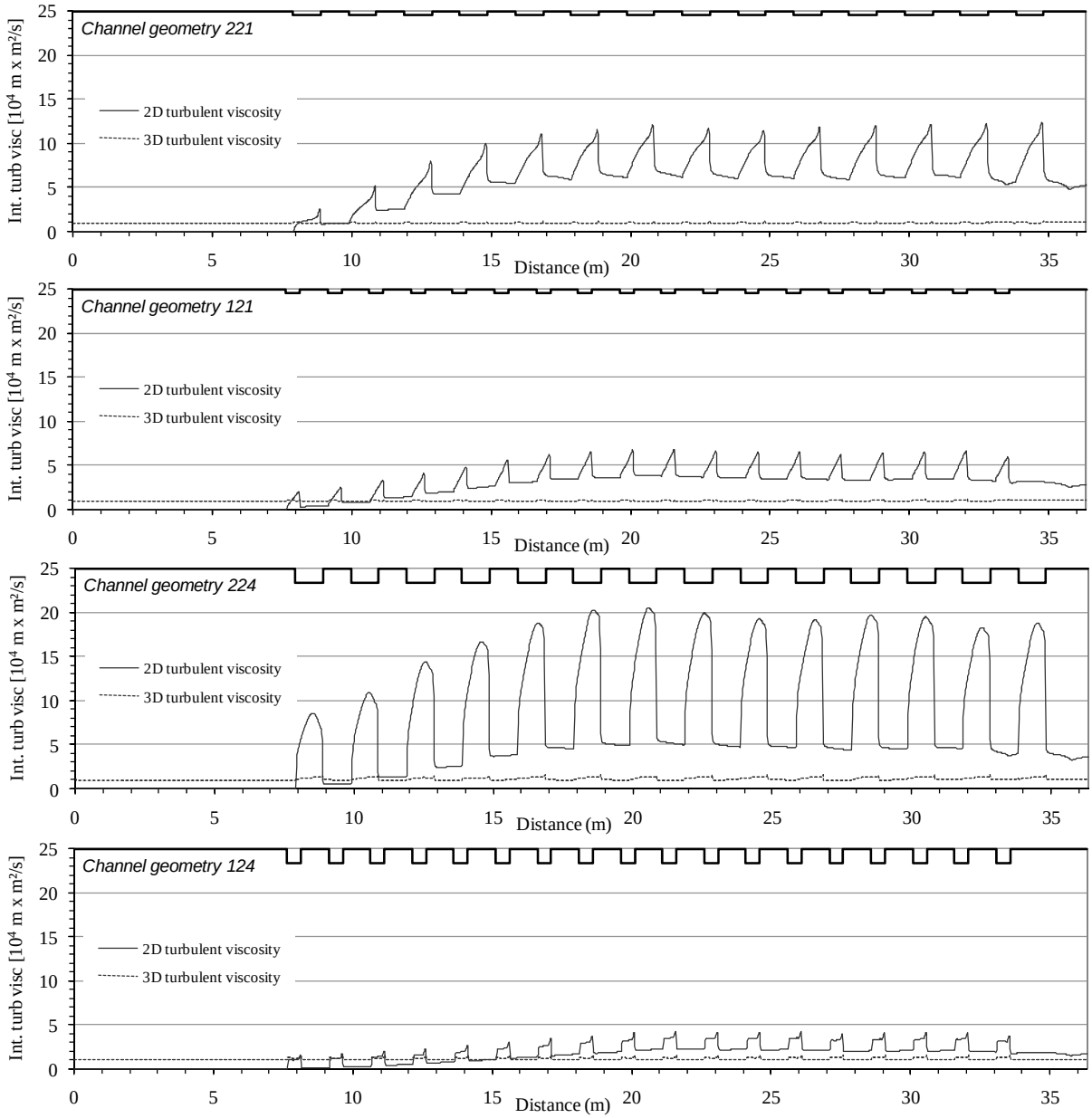

Figure 8: Evolution of the width integrated turbulent viscosity components along the channel in case of the specific discharge q_4.

Figure 9: 3D turbulent viscosity components (10^{-4} m²/s) in the upstream part of the macro-rough channel reach (7.50 m <x< 14.9 m). Configuration 221 (up) and 224 (down) with specific discharge q_4.

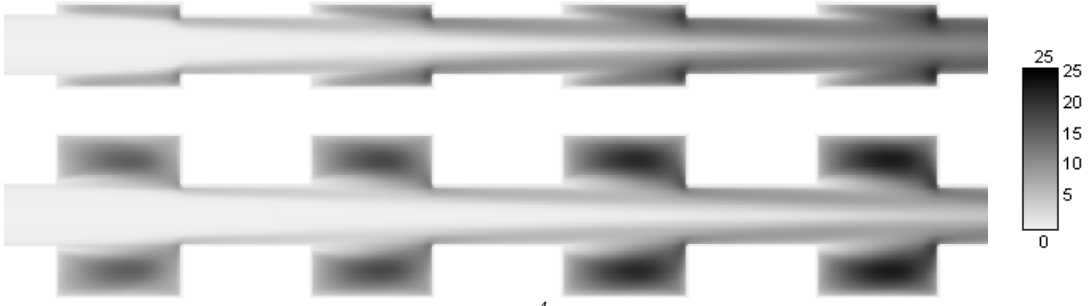

Figure 10: 2D turbulent viscosity components (10^{-4} m²/s) in the upstream part of the macro-rough channel reach (7.50 m <x< 14.9 m). Configuration 221 (up) and 224 (down) with specific discharge q_4.

Table 1: Summary of test range of geometrical parameters L_b, L_c and ΔB and derived ratios.

Cavity length L_b [m]	0.5 ; 1.0 ; 2.0
Distance between cavities L_c [m]	0.5 ; 1.0 ; 2.0
Depth of the cavity ΔB [m]	0.1 ; 0.2 ; 0.3 ; 0.4
Aspect ratio $AR = \Delta B / L_b$ [-]	0.05 ; 0.10 ; 0.15 ; 0.20 ; 0.30 ; 0.40 ; 0.60 ; 0.80
Expansion ratio $ER = (B+2\Delta B) / B$ [-]	1.41; 1.82; 2.24; 2.65

Table 2: Geometrical characteristics and specific discharges q [m^2/s] of the prismatic and the macro-rough test cases. L_b is the cavity length, L_c is the distance between cavities, ΔB is the depth of cavities, AR is the aspect ratio and ER is the expansion ratio

Case	L_b [m]	L_c [m]	ΔB [m]	AR [-]	ER [-]	q_1	q_2	q_3	q_4	q_5	q_6	q_7	q_8	q_9
Prismatic	-	-	-	-	-	.0134	.0275	.0451	.0651	.0996	.1391	.1769	.2193	.2781
221	1.0	1.0	0.1	0.1	1.41	.0100	.0229	.0367	.0708	.1006	.1317	.1731	.2149	-
121	0.5	1.0	0.1	0.2	1.41	.0114	.0245	.0404	.0726	.1033	.1300	.1762	.2189	-
224	1.0	1.0	0.4	0.4	2.65	.0108	.0238	.0396	.0693	.0999	.1343	.1738	.2186	-
124	0.5	1.0	0.4	0.8	2.65	.0130	.0218	.0397	.0719	.0971	.1311	-	-	-

* specific discharge at the flume entrance (x = 0.0 m)

Table 3: Absolute value of mean relative errors between computed and measured flow depths for all investigated geometries and specific discharges q. Errors higher than 5% are indicated in italic.

	Absolute value of mean relative error on flow depths [%]								
Geometry	q_1	q_2	q_3	q_4	q_5	q_6	q_7	q_8	q_9
Prismatic	4.2	3.8	3.9	1.8	1.8	0.8	0.9	0.8	0.7
221	3.2	*5.7*	4.3	1.5	1.0	0.8	1.1	1.3	-
121	3.4	*8.2*	3.0	2.2	3.8	2.5	1.1	0.6	-
224	*12.2*	*7.2*	3.9	4.4	*6.4*	*6.1*	*7.3*	*6.3*	-
124	*5.9*	*17.4*	*6.3*	*15.0*	*13.8*	*10.7*	-	-	-

Table 4: Absolute value of mean errors between computed and measured flow depths for all investigated geometries and specific discharges q. Errors higher than the precision of the measurements (± 2mm) are indicated in italic.

	Absolute value of mean error on flow depths [mm]								
Geometry	q_1	q_2	q_3	q_4	q_5	q_6	q_7	q_8	q_9
Prismatic	1.3	1.8	*2.6*	1.6	2.0	1.2	1.5	1.5	1.5
221	1.0	*3.2*	*3.4*	1.9	1.6	1.8	*2.9*	*4.3*	-
121	1.2	*4.3*	*2.3*	*2.9*	*7.1*	*5.4*	*2.7*	1.7	-
224	*5.0*	*4.6*	*3.5*	*6.3*	*12.5*	*14.5*	*21.3*	*21.8*	-
124	*2.5*	*10.8*	*5.6*	*21.7*	*25.4*	*23.5*	-	-	-